applied sciences

MDPI

Article

PGA Conditioning and Directional Response of Paired Earthquake Accelerograms

Sihan Yu [1], Xiaoxiang Yuan [2], Zifeng Chen [3], Jun Zhang [2], Xiaonan Zhang [4] and Qiyun Lei [1,*]

[1] Earthquake Agency of Ningxia Hui Autonomous Region, Yinchuan 750001, China
[2] Key Laboratory of Earthquake Engineering and Engineering Vibration, Institute of Engineering Mechanics, China Earthquake Administration, Harbin 150080, China
[3] Department of Hydraulic Engineering, Tsinghua University, Beijing 100084, China
[4] School of Earthquake Engineering and Building Safety, University of Emergency Management, Sanhe 065201, China
* Correspondence: leiqiyun1981@gmail.com

Abstract

Paired acceleration time histories are essential inputs to nonlinear structural analysis, but a scalar peak ground acceleration (PGA) target does not specify how the horizontal components should be scaled. This study examines the influence of amplitude conventions on paired-record processing through template reconstruction, coordinate rotation and response-spectrum calculations. A 100 s template-reconstruction dataset yields component PGAs of 350.000 and 247.510 cm/s^2, correlations with the adjusted reference of 0.988 and 0.994, and peak-normalized errors of 0.885% and 0.441%. Directional analyses use the manually processed Amatrice record pair from the Engineering Strong-Motion Database. Scaling the first rotated component to 350 cm/s^2 produces median directional PGA values between 273 and 669 cm/s^2. Applying a common factor to the pair using an RotD50 PGA target removes this dependence for rotations that preserve the tested angular grid while retaining the relative component amplitudes and temporal structure. The RotD100/RotD50 spectral ratio varies from 1.191 to 1.414 over periods of 0.05–5 s. A separate set of 240 deterministic duration-model evaluations characterizes sensitivity to magnitude, distance, site velocity and mechanism. These results demonstrate the importance of a consistent horizontal intensity definition and explicit processing metadata. Their scope is numerical verification and single-event record processing; predictive performance across earthquakes and sites requires independent evaluation.

Keywords: earthquake accelerograms; data provenance; PGA conditioning; ground motion directionality; significant duration; numerical verification

Check for updates

Academic Editors: Jae-Kwang Ahn and Suwon Son

Received: 28 September 2026
Revised: 20 October 2026
Accepted: 21 October 2026
Published: 26 October 2026

Copyright: © 2026 by the authors. Licensee MDPI, Basel, Switzerland. This article is an open access article distributed under the terms and conditions of the Creative Commons Attribution (CC BY) license.

1. Introduction

Paired recorded accelerograms are widely used as inputs to nonlinear response-history and fragility analyses [1–3]. A scalar peak ground acceleration (PGA) target alone does not specify how to scale two synchronized horizontal components: anchoring one component and targeting an orientation-independent statistic are different operations. The resulting distinction matters when directional structural demand is evaluated. Rapid RC-building vulnerability assessment can also use simplified micro-zoning procedures and neural-network surrogates [4,5], but neither approach is evaluated here.

Record selection [1–3,6], stochastic and multicomponent simulation [7–9], spectral matching [10,11], and broadband hybrid simulation [12] are established approaches to

preparing ground motions. Their predictive or engineering performance requires independent validation [13]. The potential effect of amplitude scaling on nonlinear structural drift has also been examined [14]. This study does not implement these generators or matching procedures; it examines amplitude conditioning and numerical diagnostics for supplied waveform pairs.

Directionality is a separate constraint from component-wise PGA or response-spectrum matching. Orientation-independent geometric-mean measures and the RotD family distinguish recording axes from the distribution of spectral amplitudes over azimuth [15,16]. The choice of intensity measure and horizontal input orientation can affect estimated building response [17,18]. Empirical directionality models describe changes in maximum-to-median spectral demand [19]. More recent synthesis methods prescribe RotD100 compatibility and additional directionality characteristics [20]. A fixed ratio between two component peaks does not supply these period-dependent properties, and a specified zero-lag correlation does not uniquely determine coherence, phase or polarization.

Connecting intensity fields to waveform data requires consistent acceleration units, reference site conditions, distance definitions and horizontal component conventions. Processing metadata are equally important: the sample interval, time origin and filtering history determine how records can be aligned and compared. An explicit data interface is therefore needed to link an intensity target to the selected waveform pair and to retain the information required for reproducible numerical analysis.

This study examines how the definition of a horizontal PGA target affects paired-record processing and its directional response. We use a template-reconstruction dataset to quantify waveform agreement and a processed ESM pair to evaluate common amplitude scaling, coordinate sensitivity and directional response spectra. A separate duration-model sensitivity analysis examines the role of scenario and site inputs. Together, these analyses distinguish numerical consistency within a processing workflow from the empirical representativeness of its input records.

This study does not propose a new intensity measure or establish that RotD50 is superior for predicting structural damage. Instead, it identifies a reproducibility problem in paired-record conditioning: a stated horizontal PGA target may not be the intensity actually imposed when the scaling denominator is defined on a different component convention. Using one synchronized record pair, we quantify the resulting target mismatch under coordinate rotation and specify an auditable check linking the declared target, common scaling factor, and recomputed output intensity. This is a processing-quality result, not evidence of improved structural performance; its prevalence and engineering consequences require independent records and structural-response analyses.

2. Methods

2.1. Data and Analysis Design

The analyses use two waveform datasets with distinct purposes. The template-reconstruction dataset contains a 100 s output sampled at 0.01 s, its adjusted reference and summary metrics (Table 1). Its configuration specifies a reference blend of 1.0 and a target spectrum calculated from the adjusted reference, making it an in-sample processing benchmark. The directional analysis uses the Engineering Strong-Motion Database (ESM) manually processed HGN/HGE pair for event EMSC-20160824_0000006 at station IT.AMT [21,22]. Both datasets concern the same earthquake and station but are separate processing products, not independent event samples. The prescribed 350 cm/s^2 target is a numerical test value, not a site-adjusted prediction for this event.

Table 1. Inputs and scope of the numerical analyses.

Analysis	Input and Size	Purpose
Template reconstruction	One adjusted pair; 100 s at 0.01 s spacing	Waveform agreement with the supplied template
Rotation and common scaling	One processed ESM pair; 180 angles	Coordinate sensitivity and amplitude conditioning
Response spectra	45 periods from 0.05 to 5 s; 5% damping	Directional oscillator response
Duration sensitivity	240 deterministic parameter combinations	Scenario and site dependence of model duration

The ESM headers identify M_w 6.0, normal faulting, focal depth 8.1 km, V_{S30} = 670 m/s and epicentral distance 8.5 km. Epicentral distance is not substituted for rupture distance. Both manually processed components contain 5579 synchronized samples at 0.005 s spacing, spanning 27.890 s between the first and last samples. The headers specify baseline removal and a second-order Butterworth filter with corner frequencies of 0.060 and 40 Hz. We use these processed accelerations as distributed, in cm/s^2, without an additional filter, taper or time shift. V_{S30} denotes the time-averaged shear-wave velocity in the upper 30 m.

2.2. Ground Motion Model Conventions and Units

The intensity–input interface is described using the Si-Midorikawa ground motion models (GMMs) [23,24]. These relations provide an example of the unit and component conventions that must accompany a regional target; the orientation calculations use a prescribed amplitude rather than their predictions. For the crustal branch, the PGA relation is:

$$\begin{aligned} log_{10}PGA &= 0.50M_w + 0.0043\,D \\ -log_{10}\left(R_{rup} + 0.0055 \times 10^{0.5Mw}\right) &- 0.003R_{rup} + 0.61 \end{aligned} \quad (1)$$

Equation (1) gives PGA in cm/s^2. The corresponding peak ground velocity (PGV) relation is:

$$\begin{aligned} log_{10}PGV &= 0.58M_w + 0.0038\,D \\ -log_{10}\left(R_{rup} + 0.0028 \times 10^{0.5Mw}\right) &- 0.002R_{rup} - 1.29 \end{aligned} \quad (2)$$

Equation (2) gives PGV in cm/s. M_w denotes moment magnitude, D denotes mean fault-plane depth, and R_{rup} denotes the closest distance to the rupture surface; both depth and distance are in kilometers. Mean fault-plane depth is distinct from hypocentral depth. Conversion of the predicted PGA and PGV to m/s^2 and m/s, respectively, requires division by 100.

The Si-Midorikawa relations use the larger of the two recorded horizontal peaks. Their Japanese database covers 21 earthquakes with M_w 5.8–8.3 and source depths of approximately 6–120 km, including 856 PGA and 394 PGV observations. Magnitude-dependent distance cutoffs range from 100 to 300 km. The PGA relation refers to soil sites, whereas PGV is adjusted to a stiff-site condition near V_{S30} = 600 m/s. The zero fault-type increment selects the crustal branch. These conventions define the interpretation of the predicted intensity and the conditions requiring evaluation when transferring the relations to another region.

Calculation of R_{rup} requires finite-fault geometry. Combining horizontal distance to a fault trace with a depth term is a geometric approximation and need not reproduce the distance to a dipping rupture surface. The present orientation experiment prescribes a target of 350 cm/s^2 to isolate the effect of amplitude convention from GMM and rupture-geometry assumptions.

2.3. Site Response and Aleatory Variability

A PGA site term must share the reference condition, horizontal component convention and tectonic applicability of its GMM. Integrated models such as NGA-West2 provide a framework for representing nonlinear site response, subject to regional evaluation [25,26]. A site factor defined for PGV cannot be transferred directly to PGA because the two measures have different site-response dependencies.

A conditional median is a deterministic summary, not a sampled realization, and does not describe aleatory variability. A compatible probabilistic interface is:

$$lnY_{ei} = \mu(M_w, R_{rup}, V_{S30}, mechanism, \ldots) + \tau\eta_e + \varphi\varepsilon_{ei} \quad (3)$$

Here, Y is a precisely defined horizontal intensity, μ is its predicted logarithmic median, η_e is a standardized event residual, and ε_{ei} is a standardized within-event residual. Their standard deviations τ and φ must come from the selected model. If only total dispersion σ is available, $lnY = \mu + \sigma\varepsilon$ can be used for marginal sampling, but it does not identify event and spatial dependence. A standard deviation given in base-10 logarithms is multiplied by $ln(10)$ before use in a natural-log expression. Regional realizations additionally require spatially correlated residuals [27]; independent cell-wise draws or one seed repeated over a grid is not a spatial wavefield model.

The calculations in this study use deterministic amplitude targets without sampling GMM residuals. Equation (3) defines the probabilistic input interface rather than an implemented ensemble calculation. Joint conditioning on spectral amplitude and duration would additionally require a model for their dependence.

2.4. Paired Amplitude Scaling and Orientation

Let $x_1(t)$ and $x_2(t)$ be synchronized orthogonal components. H1 and H2 identify axes; geographic north–south (NS) and east–west (EW) are used only when supported by the recording metadata. For a declared horizontal intensity functional I, the common-scaling formulation is:

$$s = Y_{target}/I[x_1, x_2], a_1(t) = sx_1(t), a_2(t) = sx_2(t) \quad (4)$$

The intensity functional in the denominator must match the target definition. The larger recorded horizontal PGA, the geometric mean of component PGAs and RotD50 PGA are distinct measures. Accordingly, a Si-Midorikawa larger-component prediction is not directly interchangeable with a RotD50 target. Applying one factor preserves the relative component amplitudes and temporal dependence of the input pair. Here, the common-scaling analysis uses a prescribed RotD50 PGA target.

$$a_\theta(t) = a_1(t)\ cos\ \theta + a_2(t)\ sin\ \theta \quad (5)$$

The orthogonal partner is $-a_1(t)\sin\theta + a_2(t)\cos\theta$. The same rotation is applied at every sample. For oscillator period T, RotD50 and RotD100 are the median and maximum of the single-direction pseudo-spectral acceleration (PSA) ordinates over $\theta \in [0°, 180°)$, respectively [16]. They are not percentiles of a geometric mean. At the acceleration level, the corresponding PGA measures use $\max|a\theta(t)|$. We evaluate 180 angles at 1° increments. This angular distribution is not an ensemble of independent records. To assess angular discretization independently of temporal sampling, we hold the 0.005 s sample interval fixed and recalculate the 5%-damped RotD50 and RotD100 PSA spectra on a 0.5° grid (360 angles). We also rotate the input pair by 17.3° and repeat the 0.5° calculation. For each measure, we report the maximum absolute relative difference over the 45 analyzed periods, using the unrotated 0.5° result at each period as the denominator.

The template-reconstruction dataset has an EW/NS peak ratio of approximately 0.70717. This ratio characterizes that dataset only. The common-scaling analysis operates on the

distributed ESM pair and retains its own component relationship, without imposing the template-reconstruction ratio.

2.5. Intercomponent Dependence

An optional correlation-control construction illustrates the distinction between imposing a scalar correlation and modeling joint horizontal motion. For a mean-removed carrier x, an independent mean-removed vector z is projected onto the subspace orthogonal to x:

$$z_{\perp} = z - x(x^T z)/(x^T x) \tag{6}$$

$$y = \rho x + (1 - \rho^2)^{1/2} \, (||x||/||z_{\perp}||) z_{\perp} \tag{7}$$

For nonzero x and $z\perp$ and $|\rho| \leq 1$, the construction gives $\mathrm{corr}(x,y) = \rho$ before further processing; degenerate vectors must be excluded. Filtering, component-dependent envelopes and spectral modification can alter this value, so correlation must be evaluated on the final output. This construction is described algebraically and is not used to generate the record pair analyzed here.

Frequency-dependent magnitude-squared coherence, $|S12(f)|^2/[S11(f)S22(f)]$, and cross-spectral phase provide information not contained in zero-lag correlation. Here, S11 and S22 are the component auto-spectral densities, and S12 is the cross-spectral density. Directional response is assessed using period-dependent RotD ratios and azimuthal oscillator response; these quantities address a different aspect of paired motion from a prescribed scalar correlation.

2.6. Duration Formulation and Assumptions

Significant duration is evaluated from the accumulated squared acceleration [28]:

$$I_A(t) \; = \; \pi/(2g) \int_0^t a^2(\tau) \, d\tau, D_{5\text{–}95} = t_{95} - t_5 \tag{8}$$

The times t_5 and t_{95} correspond to 5% and 95% of the final Arias intensity. Numerical integration uses the trapezoidal rule, followed by linear interpolation at the two thresholds. A common positive amplitude multiplier cancels from normalized Arias intensity and therefore leaves $D_{5\text{–}95}$ unchanged. A time stretch does not: it alters both duration and frequency content and requires re-evaluation of response spectra.

The optional scenario-duration branch follows the Afshari–Stewart model for active crustal regions [29]. Its median has the form:

$$D_{med} = [F_E(M_w, mechanism) + F_P(R_{rup})] \, exp(F_S + F_B) \tag{9}$$

The present sensitivity calculation sets the basin residual to zero, $F_B = 0$. The source duration F_E equals b_0 for $M_w \leq 5.2$ and $1/f_c$ otherwise. For larger magnitudes,

$$f_c = 4.9 \times 10^6 \beta \, (\Delta\sigma/M_0)^{1/3}, M_0 = 10^{1.5Mw+16.05} \tag{10}$$

Here, $\beta = 3.2$ km/s, seismic moment M_0 is in dyne cm, stress drop $\Delta\sigma$ is in bar, and f_c is in Hz. The stress parameter uses natural logarithms:

$$ln \, \Delta\sigma = b_1 + 0.9443[min(M_w,7.4) - 6] - 3.911 \, max(M_w - 7.4,0) \tag{11}$$

For normal, reverse, strike-slip and unspecified mechanisms, (b_0, b_1) is $(2.541, 3.170)$, $(1.612, 4.536)$, $(2.302, 3.467)$ and $(2.182, 3.628)$, respectively. The path and site terms are:

$$\begin{gathered} F_P(R) \; = \; 0.3165 \, min(R, \; 10) \\ + \, 0.2539 \, min[max(R - 10, \; 0), \; 40] \; + \; 0.0932 \, max(R - 50, \; 0) \end{gathered} \tag{12}$$

In Equation (12), R is in km, and F_P is in seconds.

$$F_S = -0.3183\, ln[min(V_{S30}, 600)/369.9] \quad (13)$$

The duration model predicts a horizontal geometric-mean measure. The sensitivity grid combines M_w = 5.0, 6.0, 7.0 and 7.5; R_{rup} = 0, 10, 30, 50 and 100 km; V_{S30} = 180, 360, 600 and 760 m/s; and normal, reverse and strike-slip mechanisms, giving 240 deterministic evaluations. The basin residual is set to zero throughout. This calculation is separate from the template-reconstruction dataset, which uses a calibrated duration rather than this scenario-duration branch.

For the $D_{5–95}$ branch, the natural-log event dispersion τ_D decreases linearly from 0.25 at M_w = 6.5 to 0.19 at M_w = 7.0 and is constant outside those bounds. The within-event dispersion φ_D decreases from 0.43 at M_w = 5.5 to 0.35 at M_w = 5.75, with the same clamping convention. Total dispersion is $(\tau D^2 + \varphi D^2)^{1/2}$. The interval $D_{med}\exp(\pm\sigma_D)$ shown below is a one-log-standard-deviation model interval, approximately the 16th–84th percentiles, not a confidence interval for observed performance.

2.7. Processing Verification and Response Spectra

Processing of the template-reconstruction dataset includes a prescribed onset at 15 s, acceleration-domain detrending, high-pass control and component-PGA renormalization. A reference blend of 1.0 retains the adjusted reference as the waveform template. The spectral target is calculated from that same reference. Agreement with the target and waveform therefore measures reconstruction consistency. Quiet-window acceleration is evaluated separately to describe pre-event and late-time behavior.

The template-processing implementation uses the Newmark average-acceleration method for spectral response [30]. The directional analysis of the processed ESM pair uses an exact state transition for piecewise-linear input acceleration between samples. The oscillator is initially at rest and satisfies:

$$\ddot{u} + 2\zeta\omega\dot{u} + \omega^2 u = -a(t),\ PSA(T) = \omega^2 max|u(t)| \quad (14)$$

Here, $\omega = 2\pi/T$, and ζ = 0.05. We evaluate 45 logarithmically spaced periods from 0.05 to 5 s. At each period, the two oscillator response histories are rotated before their maxima are taken. Rotating scalar component PSA values would not retain the relative timing of the responses. A harmonic-input test checks the steady-state transfer amplitude, and evaluation at half the time-step checks the sensitivity of sampled response peaks.

For the half-time-step check, each recorded acceleration component was linearly interpolated from 0.005 to 0.0025 s sampling while retaining the original start and end times (0 and 27.890 s). The same state-transition solver, 5% damping and 1° angular grid were then used. The reported PSA maxima were searched only through the final acceleration sample; post-record free vibration was not included in those spectra or in the half-step comparison. As a separate endpoint check, we propagated the terminal oscillator states for 25 s under zero input. This continuation did not change RotD50 or RotD100 at any of the 45 periods, including 5 s, for either time step in this record pair.

Template agreement is measured using the Pearson correlation coefficient and normalized root-mean-square error (NRMSE). NRMSE is the root-mean-square sample difference divided by the maximum absolute adjusted-reference acceleration, expressed as a percentage. Both measures use aligned records over the full 100 s output window. Significant duration provides a complementary measure of the timing of energy accumulation.

We performed post hoc onset-perturbation diagnostics on the distributed output and adjusted-reference histories, sampled at 0.01 s. With the upper strong-motion bound fixed at 24.00 s, we varied the lower bound from 15.00 s to 14.50 and 15.50 s and recomputed

peak-normalized NRMSE. We also computed output acceleration RMS over the nominally quiet interval from 0 s to each assumed onset. To probe comparison alignment, we shifted the output relative to the fixed reference by −0.10 and +0.10 s using linear interpolation and recomputed NRMSE over 15.00–24.00 s. These are diagnostics of window selection and comparison timing; they do not rerun onset-dependent detrending, high-pass filtering or reconstruction from the raw record.

2.8. Data Interface and Reproducibility

The regional site-input dataset contains 13,813,684 grid cells from the mainland China V_{S30} product described by Zhou et al. [31]. Its map, velocity histogram and class counts describe the spatial input available for site characterization, for which topographic slope can serve as a proxy [32]. Waveform files store time in seconds and acceleration in cm/s^2, with synchronized components on a common sample grid. Summary statistics are computed from the exported arrays and checked against their associated metadata.

3. Results

3.1. Regional Site-Input Data

The mainland China site dataset spans V_{S30} values of 107.1–1505.7 m/s (Figure 1), with a median of 382.0 m/s and a mean of 394.3 m/s (Figure 2a). The 360–760 and 180–360 m/s classes contain approximately 7.92 and 5.60 million cells, respectively. The <180 and ≥760 m/s classes contain approximately 0.17 and 0.13 million cells (Figure 2b). The two intermediate velocity classes therefore dominate the site-input distribution.

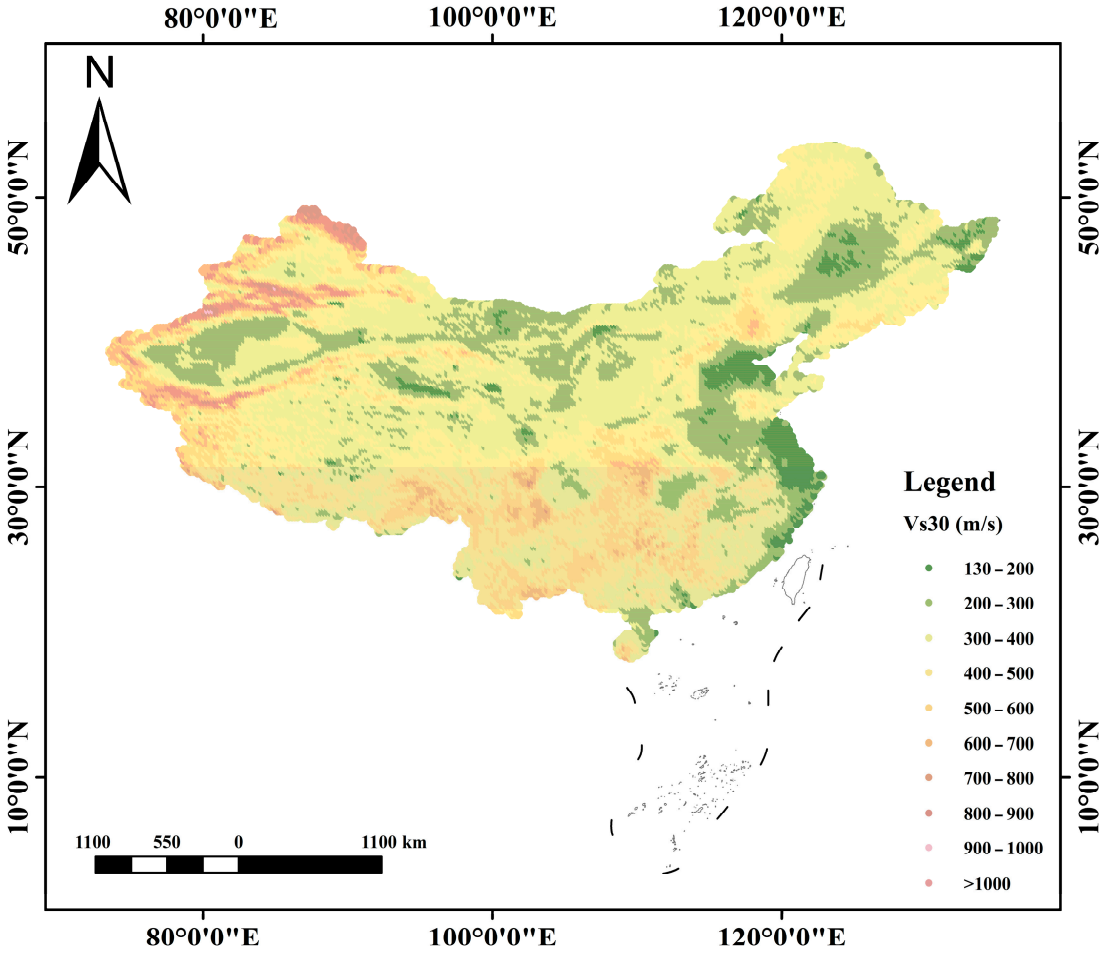


Figure 1. Mainland China V_{S30} distribution based on the site dataset described by Zhou et al. [31].

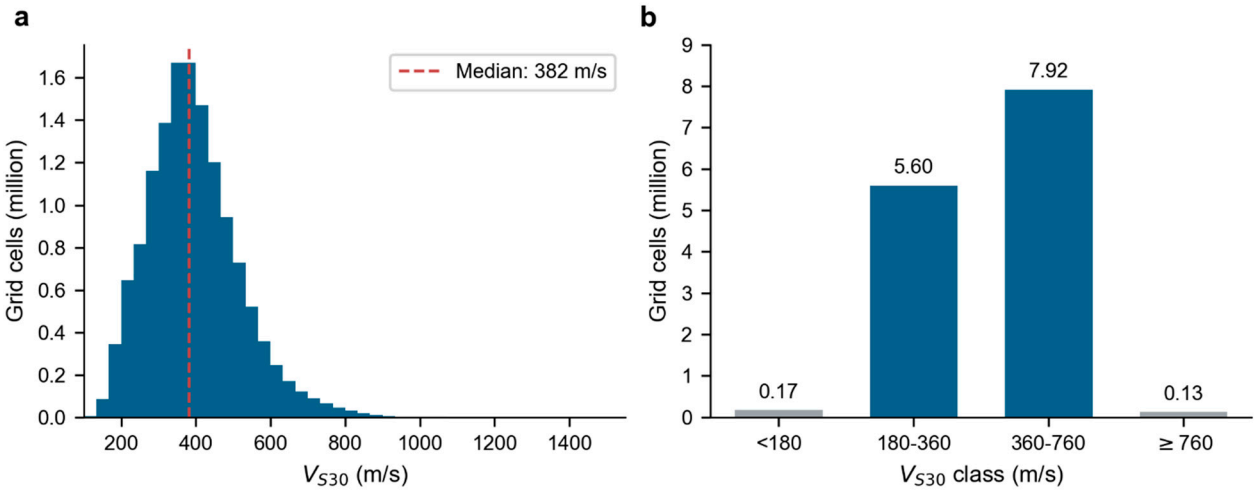


Figure 2. Regional site-input statistics from the mainland China V_{S30} dataset [31]. (**a**) Velocity histogram for 13,813,684 grid cells; the dashed line marks the median. (**b**) Cell counts in four velocity classes.

3.2. Template-Conditioned Acceleration Histories

The template-conditioned output spans 100.00 s at a sampling interval of 0.01 s, with a prescribed onset at 15.00 s (Figure 3). The NS-labeled component reaches 350.000 cm/s^2, and the EW-labeled component reaches 247.510 cm/s^2. These channel labels and their peak ratio are those of the supplied reconstruction dataset. The full records and strong-motion windows show the processed output together with its adjusted reference on a common time axis.

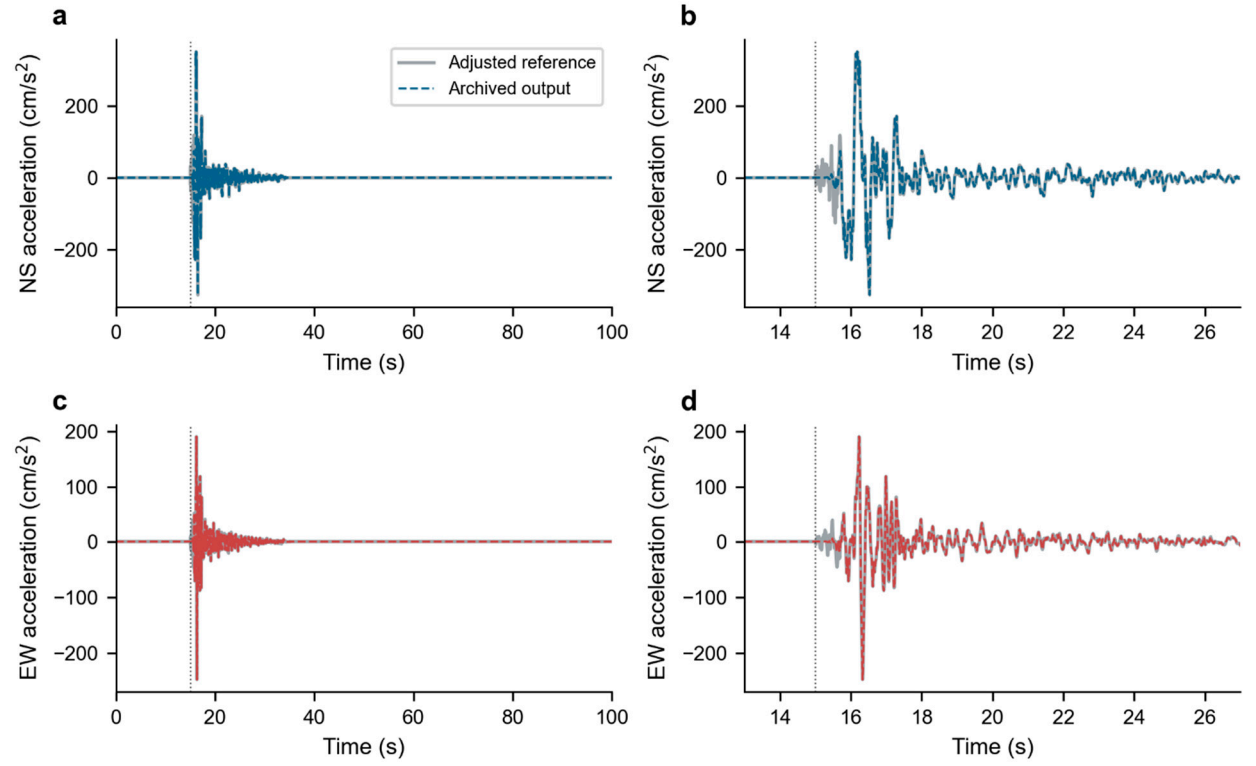


Figure 3. Template-conditioned acceleration histories. (**a**,**b**) NS-labeled output and adjusted reference over the full 100 s interval and the strong-motion interval, respectively. (**c**,**d**) Corresponding EW-labeled records. Dotted lines mark the prescribed 15 s onset.

Most of the Arias intensity accumulates shortly after the prescribed onset (Figure 4a). The output has $D_{5–95}$ values of 3.055 s for NS and 3.552 s for EW, compared with adjusted-reference durations of 3.101 and 3.734 s (Figure 4b). Acceleration root-mean-square (RMS) values are zero in the pre-event interval and approximately 0.0546 and 0.00162 cm/s^2 after 60 s (Figure 4c).

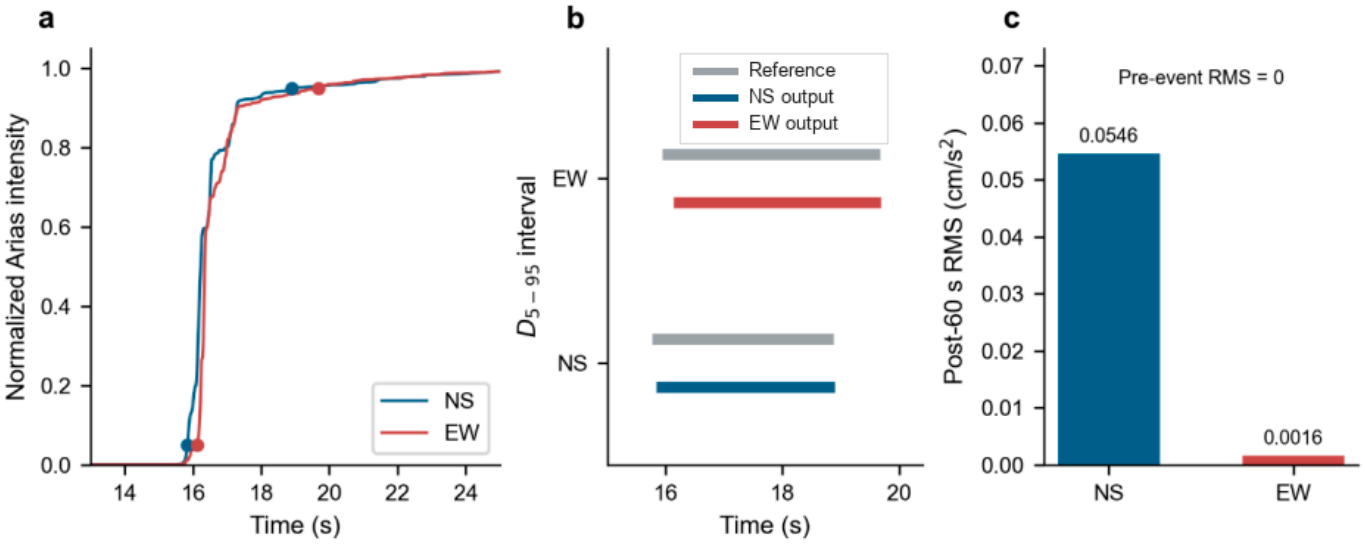


Figure 4. Energy accumulation and quiet-window acceleration for the template-conditioned output. (**a**) Normalized Arias intensity; circles mark the 5% and 95% thresholds. (**b**) $D_{5–95}$ intervals for the adjusted reference and output. (**c**) RMS acceleration after 60 s; pre-event RMS is zero for both output channels. Blue and red denote NS and EW, respectively.

3.3. Joint Horizontal Acceleration Diagnostics

The horizontal acceleration orbit shows the evolving relationship between the two components during the 15–24 s strong-motion window (Figure 5a). Vector acceleration reaches 373.5 cm/s^2 (Figure 5b). This differs from either component PGA because the component peaks need not coincide. The zero-lag correlation is 0.143, and the maximum absolute cross-correlation is 0.339 at an EW lag of 0.29 s relative to NS (Figure 5c).

3.4. Template-Reconstruction Accuracy

The output closely follows the shifted and scaled reference (Table 2). Pearson correlations are 0.988 for NS and 0.994 for EW, with peak-normalized RMS errors of 0.885% and 0.441%, respectively. Relative to the adjusted reference, output $D_{5–95}$ is shorter by approximately 1.47% for NS and 4.87% for EW. The duration differences show that high waveform correlation can coexist with measurable changes in energy-arrival timing.

Table 2. Template-reconstruction metrics.

Channel	PGA (cm/s^2)	Output $D_{5–95}$ (s)	Reference $D_{5–95}$ (s)	Correlation	NRMSE 100 s (%)	NRMSE 15–24 s (%)
NS	350.000	3.055	3.101	0.988	0.885	2.946
EW	247.510	3.552	3.734	0.994	0.441	1.470

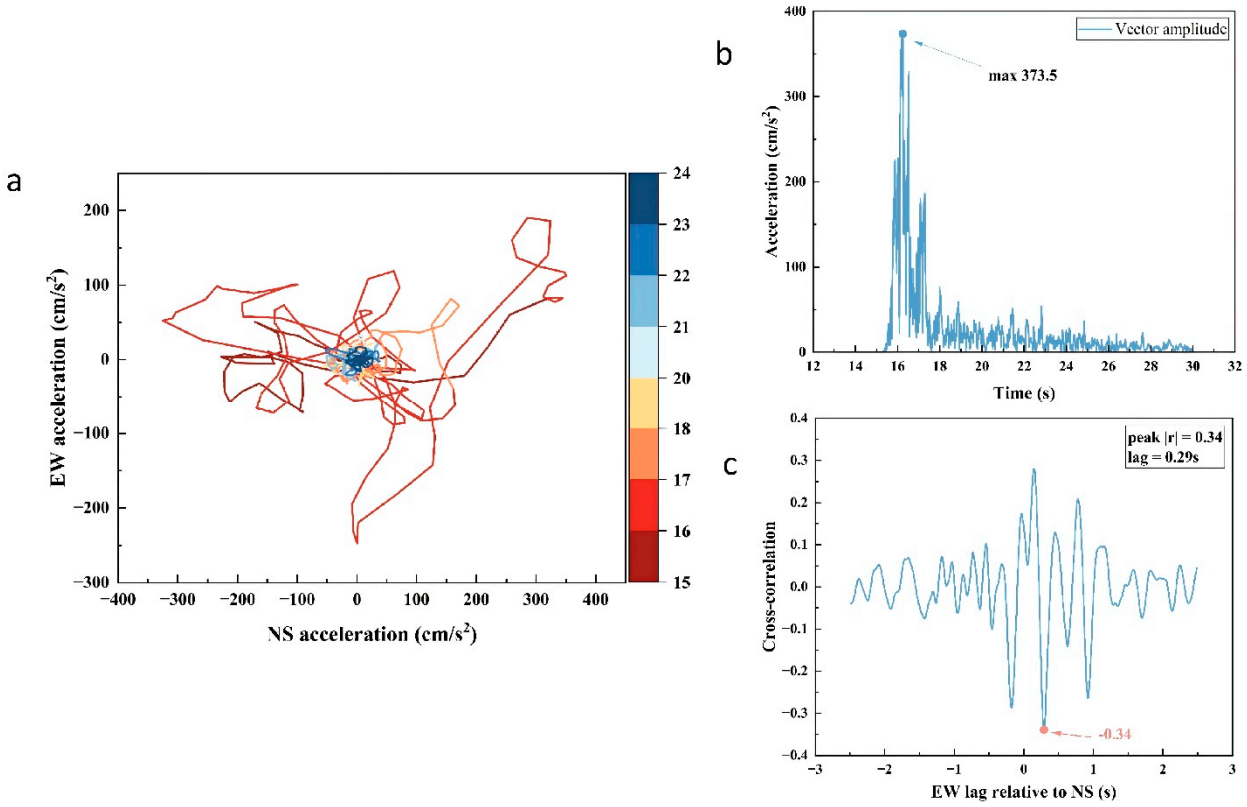


Figure 5. Joint diagnostics for the template-conditioned pair. (**a**) NS–EW acceleration orbit during 15–24 s, colored by sample time. (**b**) Vector acceleration magnitude, calculated as the square root of the sum of squared component accelerations. (**c**) Cross-correlation within the strong-motion window; the marked extremum is −0.339 at a lag of 0.29 s.

The onset-perturbation diagnostics expose sensitivity hidden by the full-record metrics. With the strong-motion upper bound fixed at 24.00 s, NRMSE for NS/EW is 2.868%/1.431%, 2.946%/1.470% and 2.364%/0.910% for lower bounds of 14.50, 15.00 and 15.50 s, respectively; each value uses the full adjusted-reference peak as denominator. The pre-onset output RMS remains zero for 14.50 and 15.00 s but becomes 0.381/0.214 cm/s^2 (NS/EW) when the assumed onset is delayed to 15.50 s. A deliberate −0.10 or +0.10 s shift of output relative to reference raises the 15.00–24.00 s NRMSE to 24.322%/22.387% or 24.453%/22.401%, respectively. These figures measure post hoc comparison sensitivity in this one supplied pair, not uncertainty in an estimated onset or the response of the original processing pipeline to a mispick.

Because the spectral target is derived from the adjusted reference, this benchmark evaluates consistency with a supplied waveform rather than agreement with an independently predicted spectrum. The following directional response results refer to the processed ESM pair and the oscillator solver described in Section 2.7.

3.5. Processed Record and Amplitude-Convention Sensitivity

The processed ESM pair has HGN and HGE PGAs of 368.387 and 850.804 cm/s^2 and $D_{5–95}$ values of 3.158 and 3.736 s, respectively (Figure 6). These distributed records provide the input for the rotation and common-scaling analyses.

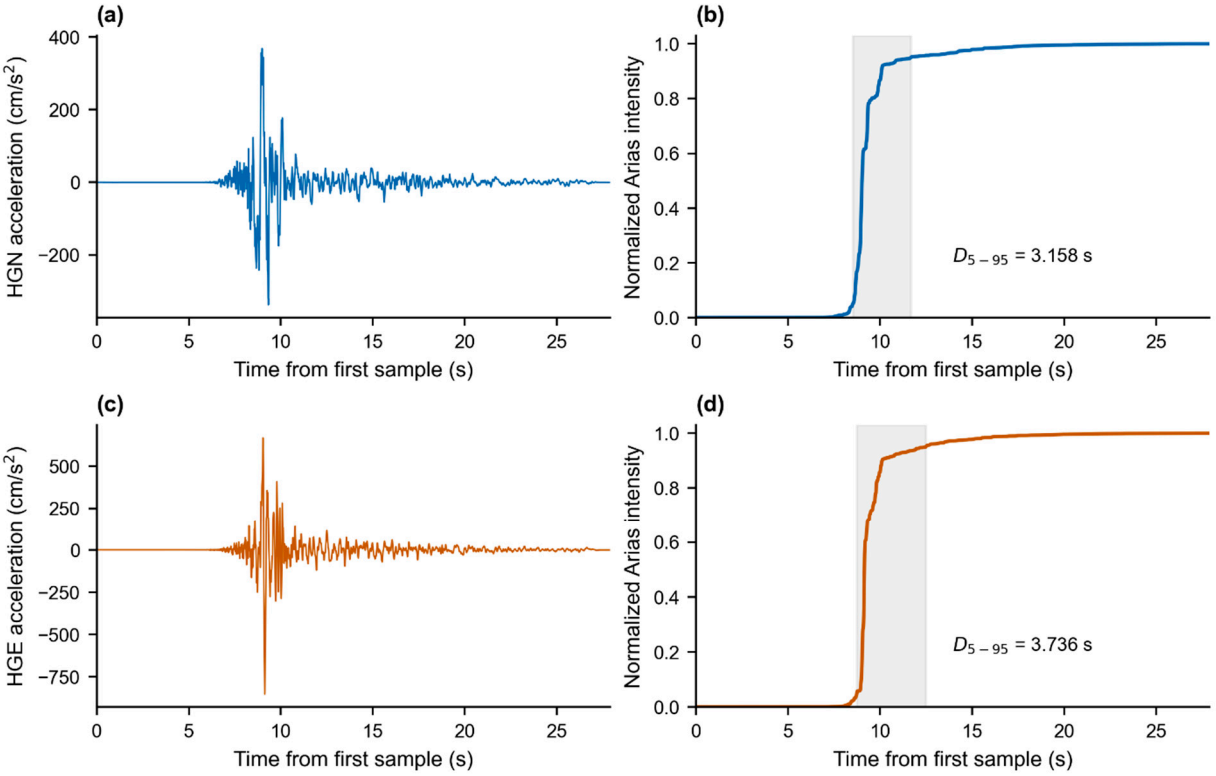


Figure 6. Processed ESM pair used for the orientation analysis. (**a**,**c**) HGN and HGE acceleration, respectively, as distributed in cm/s^2. (**b**,**d**) Corresponding normalized Arias intensity; shading marks $D_{5–95}$. Time is measured from the first sample.

The unscaled pair has RotD50 PGA = 663.651 cm/s^2 on the 1° angular grid. A common factor of 0.527385 sets this measure to 350 cm/s^2 and gives component PGAs of 194.282 and 448.701 cm/s^2. Neither individual component is required to equal the RotD50 target. By comparison, scaling the first rotated component to 350 cm/s^2 gives resulting RotD50 PGA values from 273.010 to 669.148 cm/s^2 as the axes rotate (Figure 7c), revealing the coordinate sensitivity of first-component anchoring.

3.6. Directional Response Spectra and Numerical Checks

For the processed pair, RotD100/RotD50 ranges from 1.191 to 1.414 over the analyzed periods (Figure 7a,b). Azimuthal response also varies with period (Figure 7d). A fixed component–PGA ratio therefore does not describe the full directional spectral response of this pair. Common amplitude scaling leaves the RotD100/RotD50 ratios unchanged because linear oscillator response scales by the same factor.

A 17° coordinate rotation changes the computed RotD ordinates by less than 10^{-12} in relative terms. Because this rotation permutes the 1° angular grid, the test verifies implementation consistency on that grid rather than convergence with angular resolution. At the unchanged 0.005 s sample interval, refining the angular grid from 1° to 0.5° changes RotD50 and RotD100 PSA by at most 0.179% and 0.00341%, respectively, across the 45 periods from 0.05 to 5 s. A non-integer 17.3° rotation of the input pair on the 0.5° grid changes these measures by at most 0.108% and 0.000817%, respectively, relative to the unrotated 0.5° results. These bounds characterize angular-grid sensitivity for this pair, not variability across records.

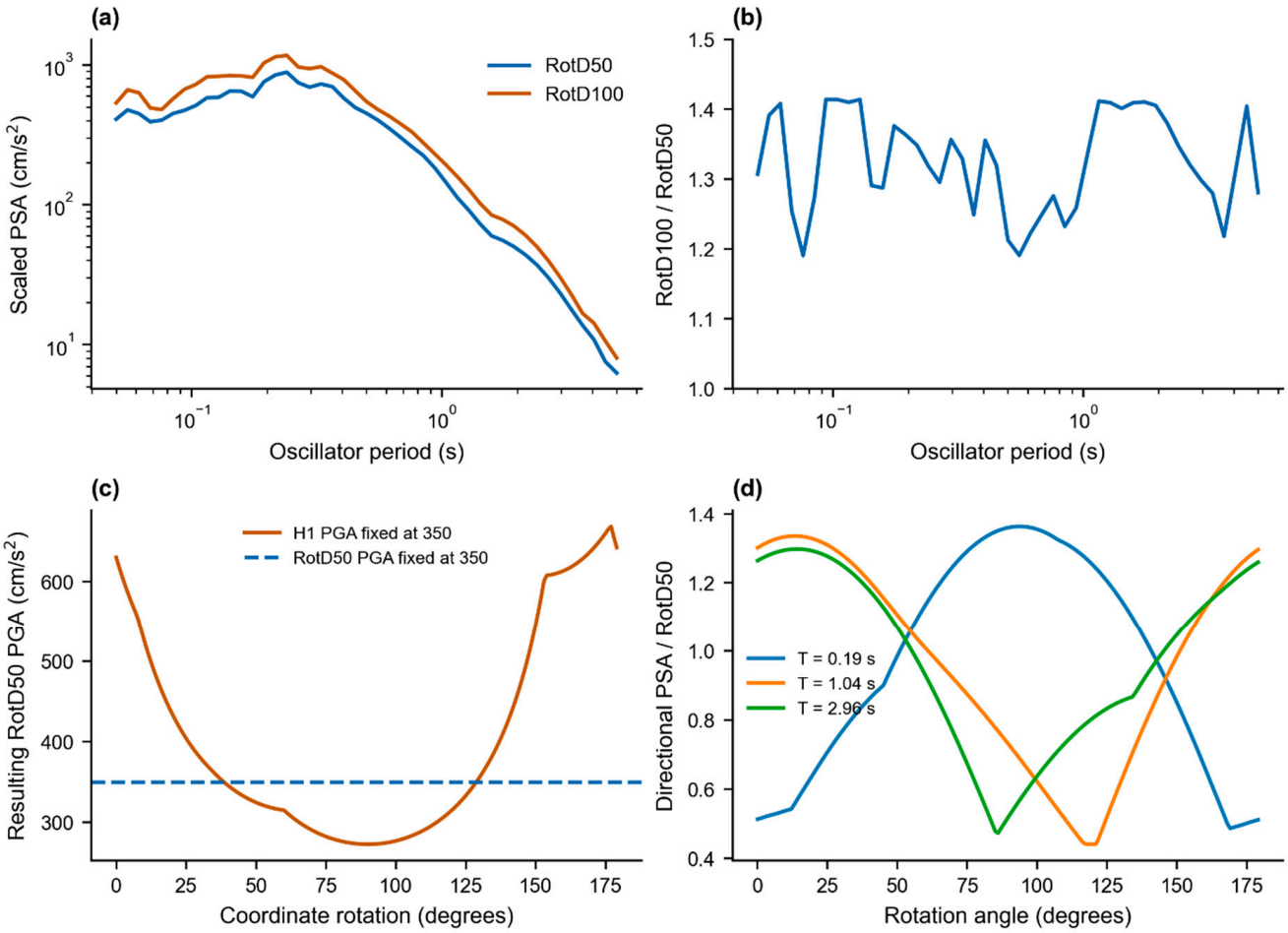


Figure 7. Directionality and amplitude conventions for the processed ESM pair. (**a**) 5%-damped RotD50 and RotD100 PSA after common scaling to RotD50 PGA = 350 cm/s^2. (**b**) Period-dependent RotD100/RotD50 ratio. (**c**) Resulting RotD50 PGA under first-component anchoring and direct RotD50 conditioning. (**d**) Angular response normalized by RotD50 at three sampled periods.

The harmonic-input amplitude error is 0.0089%. Halving the sample interval from 0.005 to 0.0025 s changes the assessed RotD ordinates by at most 0.850%, indicating limited sensitivity to the sampling of response peaks for this input.

3.7. Duration-Model Sensitivity

For $M_w = 6$, $R_{rup} = 30$ km, $V_{S30} = 360$ m/s and normal faulting, the duration model gives a median $D_{5–95}$ of 13.321 s, with zero basin residual and a total natural-log dispersion of 0.430. Figure 8 separates distance and magnitude effects from site and mechanism effects. The site contribution becomes constant at $V_{S30} = 600$ m/s by construction. The shaded range represents the model's marginal dispersion, whereas the curves describe deterministic changes in its median.

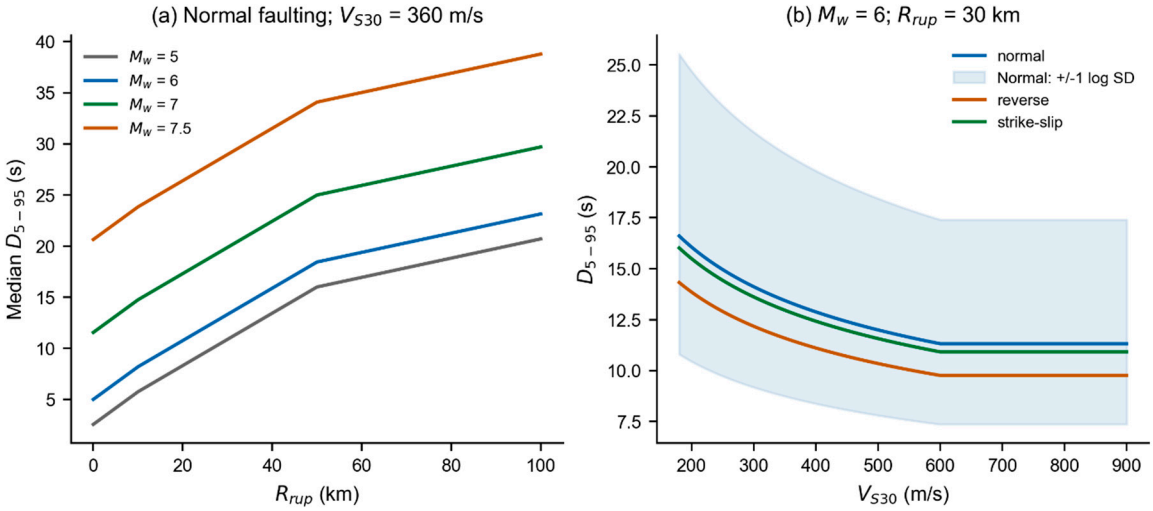


Figure 8. Significant-duration sensitivity calculated using the Afshari and Stewart [29] model with zero basin residual. (**a**) Median $D_{5–95}$ versus rupture distance at V_{S30} = 360 m/s for four magnitudes and normal faulting. (**b**) Site-velocity dependence for three mechanisms at M_w = 6 and R_{rup} = 30 km. Shading denotes the normal-faulting median multiplied by $\exp(\pm\sigma_D)$, approximately the model 16th–84th percentiles rather than confidence bounds. The discrete sensitivity grid contains 240 parameter combinations.

4. Discussion

4.1. Implications for Paired-Record Processing

The observed coordinate dependence is not a new RotD property but a consequence of defining the amplitude target on one rotated component. For the processed Amatrice pair, anchoring the first-component PGA at 350 cm/s^2 yields RotD50 PGA values of approximately 273–669 cm/s^2 across the tested rotations, whereas a common factor conditioned on RotD50 PGA controls that declared statistic by definition. This quantifies the consequence for one pair; it does not establish that RotD50 is universally preferable or improves structural-demand prediction. The scaling denominator should match the intensity measure specified for the subsequent analysis. Reporting that definition together with units, component axes, sampling and processing metadata makes the operation reproducible and prevents numerically equal but non-equivalent PGA measures from being treated as interchangeable. These considerations are pertinent to bidirectional record selection and amplitude scaling [6,14] and to studies relating intensity-measure choice and input direction to building response [17,18].

Conditioned paired accelerograms are inputs to nonlinear response-history and fragility analyses; the resulting structural demands can also enter performance-based objectives and reliability constraints in the design of seismic protection systems [33–35]. Rapid vulnerability screening through simplified micro-zoning or neural-network surrogates provides a separate assessment context [4,5], not an application tested here. For example, probabilistic optimization of bridge isolation and reliability-based optimization of adaptive sliding isolation evaluate protection-system properties under uncertain earthquake loading [33,35], while a review of seismic protection optimization covers both isolation and energy-dissipation devices [34]. Changing the horizontal-intensity or scaling convention can therefore change the input motions and potentially the computed demands, objective-function values, constraint satisfaction and selected device properties. This is an engineering implication rather than a result demonstrated here: no structural model, fragility analysis or device optimization was performed, so the direction or magnitude of any design change cannot be inferred from this single-record study.

4.2. Directionality, Duration and Baseline Behavior

For a rotation-independent intensity measure, common scaling separates the prescribed amplitude from coordinate orientation while preserving the input pair's relative amplitudes and temporal structure. The finite angular grid used here approximates that directional measure; the integer-angle rotation test checks consistency but does not establish accuracy for arbitrary grid offsets. A common factor also preserves the input waveform's limitations. Rotation changes the coordinate representation, not the underlying rupture, propagation or site effects. Representative applications therefore depend on appropriate paired-record selection.

The acceleration orbit, vector amplitude and cross-correlation complement the component PGAs by describing the simultaneous horizontal motion. The directional spectra further show that the maximum-to-median response ratio varies with period. These observations explain why a scalar correlation or component-peak ratio is insufficient to characterize joint horizontal demand. Establishing empirical multicomponent dependence would require coherence and phase analyses across a larger, scenario-relevant record set.

Baseline behavior requires assessment beyond the acceleration-domain checks reported here. Small low-frequency offsets can accumulate into velocity and displacement trends, and filtering can alter intervals outside the principal shaking window. The zero pre-event RMS and small late-time acceleration therefore do not establish negligible residual velocity or displacement. Integrated motion and filter-corner sensitivity are necessary additional checks for structural applications.

The prescribed onset is another limitation of the template benchmark. Its selection cannot be traced to a metadata pick, manual inspection or automated procedure, and an error in an operational onset could alter detrending and filtering windows, record alignment, strong-motion metrics and quiet-window diagnostics. The post hoc tests above quantify only the latter window and alignment comparisons; without the original onset-dependent preprocessing inputs and a documented picker, we cannot quantify changes in detrending or in the regenerated waveform. PhaseNet picks seismic P/S arrivals [36], while a U-Net approach detects acoustic-emission onsets in structural monitoring [37], and Earthquake Transformer combines seismic event detection and phase picking [38]. Their outputs are not interchangeable with the onset of strong shaking used here; any detector would require domain-specific validation and an uncertainty analysis before integration into this workflow.

The duration calculations describe sensitivity of the scenario model, whereas the waveform durations describe the processed records. They answer different questions: the former quantifies changes in a predicted median, and the latter measures energy accumulation in a specific time history. Setting the basin residual to zero makes the sensitivity analysis conditional on that assumption. Filtering, envelope adjustment and spectral modification can also change final-waveform duration, so imposing a model-based target would require checking the duration after all processing steps.

4.3. Applicability and Limitations

The evidence is limited to one earthquake–station pair and two processing products. The transformation connecting the template-reconstruction input to the distributed ESM pair is not fully documented in the available files; consequently, the products are analyzed separately. The reconstruction uses a calibrated reference and its own spectrum, and its full-window NRMSE includes long quiet intervals. These conditions favor close agreement and restrict the interpretation to in-sample fidelity. Independent event-separated evaluation is needed to assess performance across magnitudes, distances, sites and waveform characteristics.

This numerical comparison is not a regional ground motion application. No mainland China V_{S30} grid, Japanese ground motion model, probabilistic residual field or site-amplification relation is used to derive the prescribed target, select or modify the Amatrice pair, or infer site response. The Italian record illustrates the effect of an amplitude convention for one earthquake–station pair; it does not validate record selection or transfer to other tectonic or site conditions. Regional use would require a compatible intensity model, a representative paired-record set, and independent testing across events and sites.

5. Conclusions

This study examines PGA conditioning of paired horizontal accelerograms through waveform reconstruction, coordinate rotation and response-spectrum analysis. The template-reconstruction dataset achieves correlations of 0.988 and 0.994 and peak-normalized errors of 0.885% and 0.441%, while its significant durations differ from the adjusted reference by 1.47% and 4.87%. These complementary measures distinguish sample-wise agreement from energy-arrival timing.

For the processed Amatrice pair, fixing the first-component PGA at 350 cm/s^2 yields RotD50 PGA values of approximately 273–669 cm/s^2 over the tested rotations. Common scaling to a declared RotD50 target fixes that chosen measure while preserving the pair's period-dependent directional ratios. The numerical tests check implementation consistency, not regional predictive accuracy.

The principal limitations are that both waveform products concern the same earthquake–station pair, the template reconstruction is calibrated against its own adjusted reference and target spectrum, and the prescribed onset has no documented picking procedure. The observed directional discrepancy therefore cannot be treated as a population estimate, while reconstruction agreement does not establish out-of-sample performance. We also have not evaluated structural response or fragility, so the effect of the scaling convention on engineering demand remains unknown. Future research should validate the comparison using independent datasets from multiple earthquakes and stations across magnitude, distance, site and component-amplitude ranges; quantify sensitivity to onset and preprocessing choices; and carry the alternative amplitude conventions through nonlinear response-history and fragility analyses.

Author Contributions: S.Y.: conceptualization, methodology, software, data curation, validation, funding acquisition, and writing of the original draft and revisions. Q.L.: literature review, original drafting, funding acquisition, and manuscript revision. X.Y.: formal analysis, methodology, resources, supervision, and manuscript revision. Z.C.: investigation, methodology, and manuscript revision. J.Z.: literature review, original drafting, and manuscript revision. X.Z.: data curation, original drafting, and manuscript revision. All authors have read and agreed to the published version of the manuscript.

Funding: This work was supported by the Key R&D Program Key Projects of Ningxia Hui Autonomous Region (2024BEG02033; 2026BEG02074); the Ningxia Natural Science Foundation Key Project (2026AAC020064) and Active Fault Investigation and Hazard Assessment Project in Zhongwei City.

Data Availability Statement: The ESM input is identified by event EMSC-20160824_0000006, network IT, station AMT, streams HGN and HGE, and the manually processed acceleration product [22]. Regional site-grid summaries are derived from the mainland China dataset described by Zhou et al. [31]; the complete grid is not redistributed.

Conflicts of Interest: The authors declare no conflict of interest.

References

1. Bommer, J.J.; Acevedo, A.B. The use of real earthquake accelerograms as input to dynamic analysis. *J. Earthq. Eng.* **2004**, *8*, 43–91. [CrossRef]
2. Katsanos, E.I.; Sextos, A.G.; Manolis, G.D. Selection of earthquake ground motion records: A state-of-the-art review from a structural engineering perspective. *Soil Dyn. Earthq. Eng.* **2010**, *30*, 157–169. [CrossRef]
3. Baker, J.W. Conditional Mean Spectrum: Tool for Ground-Motion Selection. *J. Struct. Eng.* **2011**, *137*, 322–331. [CrossRef]
4. Zona, R.; Imani, H.; Losco, S.; Modano, M.; Minutolo, V. Fast evaluation of seismic vulnerability of RC building: A proposal of micro-zoning procedure for safety assessment. *Nat. Hazards* **2025**, *121*, 23329–23347. [CrossRef]
5. Forooghi, A.; Imani, H.; Minutolo, V.; Zona, R. Multi-Output Neural Network for Elastic and Collapse Multipliers Prediction in Structural Vulnerability Assessment. *Int. J. Struct. Stab. Dyn.* **2026**, *26*, 2750319. [CrossRef]
6. Beyer, K.; Bommer, J.J. Selection and Scaling of Real Accelerograms for Bi-Directional Loading: A Review of Current Practice and Code Provisions. *J. Earthq. Eng.* **2007**, *11*, 13–45. [CrossRef]
7. Boore, D.M. Simulation of Ground Motion Using the Stochastic Method. *Pure Appl. Geophys.* **2003**, *160*, 635–676. [CrossRef]
8. Rezaeian, S.; Der Kiureghian, A. Simulation of synthetic ground motions for specified earthquake and site characteristics. *Earthq. Eng. Struct. Dyn.* **2010**, *39*, 1155–1180. [CrossRef]
9. Rezaeian, S.; Der Kiureghian, A. Simulation of orthogonal horizontal ground motion components for specified earthquake and site characteristics. *Earthq. Eng. Struct. Dyn.* **2012**, *41*, 335–353. [CrossRef]
10. Hancock, J.; Watson-Lamprey, J.; Abrahamson, N.A.; Bommer, J.J.; Markatis, A.; McCoy, E.; Mendis, R. An improved method of matching response spectra of recorded earthquake ground motion using wavelets. *J. Earthq. Eng.* **2006**, *10*, 67–89. [CrossRef]
11. Al Atik, L.; Abrahamson, N. An Improved Method for Nonstationary Spectral Matching. *Earthq. Spectra* **2010**, *26*, 601–617. [CrossRef]
12. Graves, R.W.; Pitarka, A. Broadband Ground-Motion Simulation Using a Hybrid Approach. *Bull. Seismol. Soc. Am.* **2010**, *100*, 2095–2123. [CrossRef]
13. Galasso, C.; Zareian, F.; Iervolino, I.; Graves, R.W. Validation of Ground-Motion Simulations for Historical Events Using SDoF Systems. *Bull. Seismol. Soc. Am.* **2012**, *102*, 2727–2740. [CrossRef]
14. Luco, N.; Bazzurro, P. Does amplitude scaling of ground motion records result in biased nonlinear structural drift responses? *Earthq. Eng. Struct. Dyn.* **2007**, *36*, 1813–1835. [CrossRef]
15. Boore, D.M.; Watson-Lamprey, J.; Abrahamson, N.A. Orientation-Independent Measures of Ground Motion. *Bull. Seismol. Soc. Am.* **2006**, *96*, 1502–1511. [CrossRef]
16. Boore, D.M. Orientation-Independent, Nongeometric-Mean Measures of Seismic Intensity from Two Horizontal Components of Motion. *Bull. Seismol. Soc. Am.* **2010**, *100*, 1830–1835. [CrossRef]
17. Aquib, T.A.; Sivasubramonian, J.; Mai, P.M. Analysis of Ground Motion Intensity Measures and Selection Techniques for Estimating Building Response. *Appl. Sci.* **2022**, *12*, 12089. [CrossRef]
18. Bugueño, I.; Carvallo, J.; Vielma, J.C. Influence of Directionality on the Seismic Response of Typical RC Buildings. *Appl. Sci.* **2022**, *12*, 1534. [CrossRef]
19. Shahi, S.K.; Baker, J.W. NGA-West2 Models for Ground Motion Directionality. *Earthq. Spectra* **2014**, *30*, 1285–1300. [CrossRef]
20. Zhou, J.; Shen, S.D.; Igarashi, A.; He, X.H. Generation of synthetic spectrum-compatible bi-directional ground motions with specific directionality. *Soil Dyn. Earthq. Eng.* **2024**, *186*, 108893. [CrossRef]
21. Luzi, L.; Puglia, R.; Russo, E.; D'Amico, M.; Felicetta, C.; Pacor, F.; Lanzano, G.; Çeken, U.; Clinton, J.; Costa, G.; et al. The Engineering Strong-Motion Database: A Platform to Access Pan-European Accelerometric Data. *Seismol. Res. Lett.* **2016**, *87*, 987–997. [CrossRef]
22. Mascandola, C.; Felicetta, C.; Russo, E.; Luzi, L.; Lanzano, G.; Sgobba, S.; Brunelli, G.; Ramadan, F.; Pacor, F.; ORFEUS Strong-Motion SMC. *Engineering Strong Motion Database (ESM), Version 3.0*; Istituto Nazionale di Geofisica e Vulcanologia: Rome, Italy, 2026. [CrossRef]
23. Si, H.; Midorikawa, S. New attenuation relationships for peak ground acceleration and velocity considering effects of fault type and site condition. *J. Struct. Constr. Eng.* **1999**, *64*, 63–70. [CrossRef]
24. Si, H.; Midorikawa, S. New attenuation relations for peak ground acceleration and velocity considering effects of fault type and site condition. In *Proceedings of the 12th World Conference on Earthquake Engineering, Auckland, New Zealand, 30 January–4 February 2000*; New Zealand Society for Earthquake Engineering: Wellington, New Zealand, 2000; Paper 0532. Available online: https://wcee.nicee.org/wcee/article/0532.pdf (accessed on 20 October 2026).
25. Boore, D.M.; Stewart, J.P.; Seyhan, E.; Atkinson, G.M. NGA-West2 Equations for Predicting PGA, PGV, and 5% Damped PSA for Shallow Crustal Earthquakes. *Earthq. Spectra* **2014**, *30*, 1057–1085. [CrossRef]
26. Seyhan, E.; Stewart, J.P. Semi-Empirical Nonlinear Site Amplification from NGA-West2 Data and Simulations. *Earthq. Spectra* **2014**, *30*, 1241–1256. [CrossRef]

27. Jayaram, N.; Baker, J.W. Correlation model for spatially distributed ground-motion intensities. *Earthq. Eng. Struct. Dyn.* **2009**, *38*, 1687–1708. [CrossRef]
28. Arias, A. A measure of earthquake intensity. In *Seismic Design for Nuclear Power Plants*; Hansen, R.J., Ed.; MIT Press: Cambridge, MA, USA, 1970; pp. 438–483.
29. Afshari, K.; Stewart, J.P. Physically Parameterized Prediction Equations for Significant Duration in Active Crustal Regions. *Earthq. Spectra* **2016**, *32*, 2057–2081. [CrossRef]
30. Newmark, N.M. A Method of Computation for Structural Dynamics. *J. Eng. Mech. Div.* **1959**, *85*, 67–94. [CrossRef]
31. Zhou, J.; Li, L.; Li, X.; Xi, N.; Tian, X. A 30 Arcsec Resolution VS30 Map for Mainland China Using Refined Topographic Slope-Based Cokriging (SCK) Model. *Bull. Seismol. Soc. Am.* **2025**, *115*, 332–348. [CrossRef]
32. Wald, D.J.; Allen, T.I. Topographic Slope as a Proxy for Seismic Site Conditions and Amplification. *Bull. Seismol. Soc. Am.* **2007**, *97*, 1379–1395. [CrossRef]
33. Li, Y.; Conte, J.P. Probabilistic performance-based optimum design of seismic isolation for a California high-speed rail prototype bridge. *Earthq. Eng. Struct. Dyn.* **2018**, *47*, 497–514. [CrossRef]
34. Marano, G.C.; Rosso, M.M.; Melchiorre, J. Optimization as a Tool for Seismic Protection of Structures. In *Seismic Isolation, Energy Dissipation and Active Vibration Control of Structures*; Lecture Notes in Civil Engineering; Springer: Cham, Switzerland, 2023; Volume 309, pp. 100–113. [CrossRef]
35. Peng, Y.; Ma, Y.; Huang, T.; De Domenico, D. Reliability-based design optimization of adaptive sliding base isolation system for improving seismic performance of structures. *Reliab. Eng. Syst. Saf.* **2021**, *205*, 107167. [CrossRef]
36. Zhu, W.; Beroza, G.C. PhaseNet: A deep-neural-network-based seismic arrival-time picking method. *Geophys. J. Int.* **2019**, *216*, 261–273. [CrossRef]
37. Melchiorre, J.; D'Amato, L.; Agostini, F.; Rizzo, A.M. Acoustic emission onset time detection for structural monitoring with U-Net neural network architecture. *Dev. Built Environ.* **2024**, *18*, 100449. [CrossRef]
38. Mousavi, S.M.; Ellsworth, W.L.; Zhu, W.; Chuang, L.Y.; Beroza, G.C. Earthquake transformer: An attentive deep-learning model for simultaneous earthquake detection and phase picking. *Nat. Commun.* **2020**, *11*, 3952. [CrossRef]

Disclaimer/Publisher's Note: The statements, opinions and data contained in all publications are solely those of the individual author(s) and contributor(s) and not of MDPI and/or the editor(s). MDPI and/or the editor(s) disclaim responsibility for any injury to people or property resulting from any ideas, methods, instructions or products referred to in the content.